

## Biofouling

The Journal of Bioadhesion and Biofilm Research

ISSN: 0892-7014 (Print) 1029-2454 (Online) Journal homepage: <https://www.tandfonline.com/loi/gbif20>

# Roughness effects of diatomaceous slime fouling on turbulent boundary layer hydrodynamics

Elizabeth A. K. Murphy, Julio M. Barros, Michael P. Schultz, Karen A. Flack, Cecily N. Steppe & Matthew A. Reidenbach

To cite this article: Elizabeth A. K. Murphy, Julio M. Barros, Michael P. Schultz, Karen A. Flack, Cecily N. Steppe & Matthew A. Reidenbach (2019): Roughness effects of diatomaceous slime fouling on turbulent boundary layer hydrodynamics, *Biofouling*, DOI: [10.1080/08927014.2018.1517867](https://doi.org/10.1080/08927014.2018.1517867)

To link to this article: <https://doi.org/10.1080/08927014.2018.1517867>



Published online: 03 Jan 2019.



Submit your article to this journal [↗](#)



Article views: 110



View Crossmark data [↗](#)



## Roughness effects of diatomaceous slime fouling on turbulent boundary layer hydrodynamics

Elizabeth A. K. Murphy<sup>a</sup> , Julio M. Barros<sup>b\*</sup> , Michael P. Schultz<sup>c</sup>, Karen A. Flack<sup>d</sup>, Cecily N. Steppe<sup>e</sup> and Matthew A. Reidenbach<sup>f</sup> 

<sup>a</sup>Department of Environmental Sciences, University of Virginia, Charlottesville, VA, USA; <sup>b</sup>Department of Mechanical Engineering, United States Naval Academy, Annapolis, MD, USA; <sup>c</sup>Department of Naval Architecture and Ocean Engineering, United States Naval Academy, Annapolis, MD, USA; <sup>d</sup>Department of Mechanical Engineering, United States Naval Academy, Annapolis, MD, USA; <sup>e</sup>Department of Oceanography, United States Naval Academy, Annapolis, MD, USA; <sup>f</sup>Department of Environmental Sciences, University of Virginia, Charlottesville, VA, USA

### ABSTRACT

Biofilm fouling significantly impacts ship performance. Here, the impact of biofilm on boundary layer structure at a ship-relevant, low Reynolds number was investigated. Boundary layer measurements were performed over slime-fouled plates using high resolution particle image velocimetry (PIV). The velocity profile over the biofilm showed a downward shift in the log-law region ( $\Delta U^+$ ), resulting in an effective roughness height ( $k_s$ ) of 8.8 mm, significantly larger than the physical thickness of the biofilm ( $1.7 \pm 0.5$  mm) and generating more than three times as much frictional drag as the smooth-wall. The skin-friction coefficient,  $C_f$ , of the biofilm was  $9.0 \times 10^{-3}$  compared with  $2.9 \times 10^{-3}$  for the smooth wall. The biofilm also enhances turbulent kinetic energy (*tke*) and Reynolds shear stress, which are more heterogeneous in the streamwise direction than smooth-wall flows. This suggests that biofilms increase drag due to high levels of momentum transport, likely resulting from protruding streamers and surface compliance.

### ARTICLE HISTORY

Received 21 February 2018  
Accepted 25 August 2018

### KEYWORDS

Biofilm; turbulence; drag; roughness; PIV; boundary layer

### Introduction

Aquatic surfaces, especially man-made surfaces such as ships' hulls, tidal turbine blades and the walls of pipes, often become rough due to the attachment and growth of organisms (biofouling). This roughness typically reduces the performance of such engineered systems (Picologlou et al. 1980; Lewthwaite et al. 1985; Towsin 2003; Walker et al. 2013a). Surface roughness due to biofouling on ships' hulls has major economic consequences for shipping and naval activities. For example, for a single class of mid-sized surface vessels alone, biofouling costs the US Navy an estimated \$56 million per year due to increased fuel consumption and expenses associated with cleaning and painting the hull (Schultz et al. 2011). Fouling-release (FR) and antifouling (AF) hull coatings can help control hard fouling, such as barnacles. However, these coatings are often ineffective at preventing slime fouling (Molino & Wetherbee 2008).

The primary biofouling community seen on US Navy vessels is biofilm fouling (Schultz et al. 2015). This thin soft-fouling community, also called slime, is found on most aquatic surfaces and tends to be one of the first types of fouling to occur. On ships' hulls, biofilms are primarily composed of bacterial cells and diatoms, a unicellular algae, embedded in viscoelastic extracellular polymeric substances (EPS) (Stoodley et al. 1999; Hunsucker et al. 2018). Diatoms are typically the dominant species in a biofilm, and the abundance and diversity of the diatom fouling community depends on the geographic location, local hydrodynamics and the type of surface being colonized (Zargiel et al. 2011; Hunsucker et al. 2014; Zargiel & Swain 2014). The species assemblage composing a biofilm, as well as the hydrodynamic regime in which it grows, determines a biofilm's physical structure. Diverse biofilm species have distinctive cell surface properties (ie hydrophobicity or

CONTACT Elizabeth Murphy  eam6vf@virginia.edu

Current affiliation: Julio M. Barros  juliomanuel.barrosjunior@oist.jp Fluid Mechanics Unit, Okinawa Institute of Science and Technology, Okinawa, Japan 904-0495.

This work was authored as part of the Contributor's official duties as an Employee of the United States Government and is therefore a work of the United States Government. In accordance with 17 U.S.C. 105, no copyright protection is available for such works under U.S. Law

hydrophilicity) that may influence how the structures interact with the flow within the turbulent boundary layer above the biofilm (de Beer & Kühn 2001). Biofilm thicknesses range from micrometers to millimeters, and the structure of biofilms is highly heterogeneous, often composed of bulbous cell clusters between which are voids that permit fluid flow (de Beer et al. 1996). When grown under shear, biofilms form thin, flexible streamers that protrude from the surface (Taherzadeh et al. 2009).

The Naval Ships' Technical Manual (US Navy 2006) assumes that soft fouling, such as a biofilm, results in minimal reduction in ship performance. Therefore, soft fouling found during a hull inspection is not considered a reason to clean the hull. However, recent work shows that although biofilms typically have low vertical relief and are compliant, biofilm fouling can induce a steep drag penalty on fouled surfaces. For example, Schultz et al. (2015) indicate that slime fouling can increase the skin friction up to 70% in a laboratory-scale turbulent channel flow. This corresponds to approximately a 10% increase in the required propulsive power for a mid-sized naval surface combatant at cruising speed. Field and laboratory trials indicate that slime on ships' hulls significantly increases the resistance and power requirements of the vessel (Haslbeck & Bohlander 1992; Schultz 2007). Therefore, it is important to understand the interactions between biofilms and boundary layer flow in order to better assess the impacts of slime fouling on ship performance.

Fouling affects ship performance by increasing the roughness of the hull surface. Most studies of the effects of roughness on the turbulent boundary layer focus on rigid roughness elements, often with regular spacing (Krogstad & Antonia 1999; Flack et al. 2005; Flack & Schultz 2010). However, in biological systems, compliance and irregularity are the norm. Under some wall boundary conditions, a compliant surface can decrease skin friction by lessening the intensity of turbulence near the wall and reducing the amount of energy carried in streamwise vortices (Xu et al. 2003). Some studies of biofilms and other types of algal growth on already-rough surfaces such as coral reefs or pebble beds, show a reduction in surface roughness as well as a decrease in bed shear stresses compared to the bare roughness elements because the biofilm growth effectively smooths out the surface (Nikora et al. 2002; Graba et al. 2010; Stocking et al. 2016). However, direct measurements show that biofilms can also increase skin friction when they grow on smoother surfaces, such as ships'

hulls (Swain et al. 2007; Munk et al. 2009), and analysis of the mean velocity profile over biofilms shows that the effective roughness height ( $k_s$ ) of the fouled surface can be significantly greater than the physical height of the biofilm itself (Walker et al. 2013b). The effective roughness height is a measure of the magnitude of the roughness effect on the boundary layer, in terms of the diameter of close-packed sand grains that would result in the equivalent momentum extraction from the flow (Nikuradse 1933).

Given that biofilms can show a large increase in skin friction despite a small physical roughness height, this study examined the spatially explicit effects of a biofilm on the friction velocity, turbulent kinetic energy, instantaneous momentum transport, vortical motion, and coherent structures within the turbulent boundary layer. The goal of this work was to investigate how biofilm fouling alters the turbulent boundary layer and to better understand why biofilms induce such steep drag penalties. In order to assess both the average velocity field over a biofilm as well as the heterogeneous nature of turbulence parameters over a natural living surface, high resolution 2-D particle image velocimetry (PIV) measurements were obtained in the boundary layer of a low Reynolds number flow. Preliminary results from this study were presented in Murphy et al. (2017). The results presented are for a large, uniformly-fouled plate with relatively thick biofilm fouling. Both the velocity field throughout the boundary layer, and the spatially-resolved generation of turbulent and shear stresses were measured, and therefore provide insights into the interactions of biofilms with turbulent boundary layer flow.

## Materials and methods

### Biofilm and facilities

A dynamic slime exposure facility, described in Schultz et al. (2015), was used to grow biofilm on large (0.20 m × 1.52 m) acrylic plates fixed to the outside of a rotating drum submerged in brackish water with a salinity of 18 ppt. The drum rotated at 60 rpm, creating a peripheral velocity of  $1.9 \text{ m s}^{-1}$ , so that biofilm growth occurred under shear. The biofilm consisted of four genera of diatoms (*Amphora*, *Achnanthes*, *Entomoneis* and *Navicula*) that are commonly found on ships, and are also found on AF and FR coatings that have been exposed to the marine environment under dynamic conditions (Zargiel et al. 2011; Schultz et al. 2015). The fouled plate was exposed in the dynamic slime facility for 10 weeks and had a fairly uniform layer of biofilm

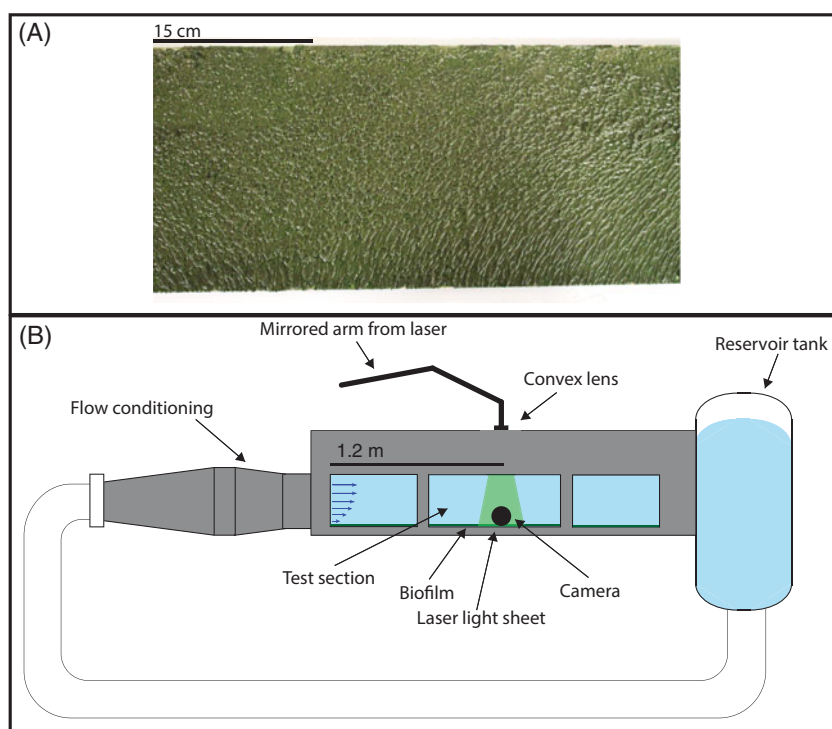


**Figure 1.** (A) A portion of the fouled acrylic plate used in this study, photographed in air and (B) a schematic of the tunnel flow facility, not to scale.

that averaged  $1.7 \pm 0.5$  mm thick with a mean peak-to-trough distance of 0.5 mm. The biofilm thickness measurements were made on the wet biofilm in air using a wet film thickness paint gauge, as outlined in Schultz et al. (2015). An image of the biofilm used in this study is given in Figure 1A.

Testing was performed in a recirculating tunnel facility in the US Naval Academy Hydromechanics Laboratory (Figure 1B). The flow enters the test section through several flow-conditioning devices: a contraction, mesh screens and a honeycomb flow straightener. The freestream turbulence in this facility was  $<0.5\%$  (Volino et al. 2007). The test section of the tunnel was  $0.2 \text{ m} \times 0.1 \text{ m}$ , with a length of 2 m. The adjustable top wall of the tunnel was set to provide a zero-pressure gradient flow during testing. The free stream velocity was  $1.1 \text{ m s}^{-1}$ . Naval ships, where these biofilms are common, typically cruise at  $7.7 \text{ m s}^{-1}$ , with a maximum speed of around  $15.4 \text{ m s}^{-1}$  (Schultz 2007). The fluid-structure interaction of the biofilm within the authors' test facility could be different compared to the dynamics of a fully developed boundary layer over a ship at high speed. However, the very low stiffness of the biofilm streamers (Young's modulus is around  $5,000 \text{ kg m}^{-1}\text{s}^{-2}$  (Taherzadeh et al. 2009)), suggests that the biofilms were near or at full deformation at even the moderate speeds in the present flow tunnel, so the

reconfiguration, or posture, of the streamers would not likely change significantly at higher velocities. Additionally, the flapping frequency of the streamers is expected to be similar between the flow tunnel and real-world conditions, because flapping frequency appears to be dependent on flow velocity only to around  $25 \text{ cm s}^{-1}$  (Stoodley et al. 1998).

Particle image velocimetry (PIV) was used to capture the flow field in the streamwise - wall-normal ( $x-y$ ) plane. The system consisted of one  $6.6\text{k} \times 4.4\text{k}$  pixels 12 bit frame straddle CCD camera (TSI 29MP) coupled with a 190 mJ per pulse, dual-cavity pulsed Nd:YAG laser (Quantel). A 0.3 mm thick laser light-sheet was formed by a spherical-cylindrical lens configuration. The flow was seeded with  $2 \mu\text{m}$  silver coated glass-sphere particles, and all measurements were performed  $\sim 1.22 \text{ m}$  downstream of the boundary layer trip, and  $\sim 0.42 \text{ m}$  downstream of the leading edge of the fouled plate. The time-delay,  $dt$ , between the image-pairs was  $250 \mu\text{s}$ . The time-delayed images were interrogated using a recursive two-frame cross-correlation methodology, with a final pass of  $32^2$  pixels with 50% overlap to satisfy the Nyquist sampling criterion (Insight 4G version 11). Statistical validation tools were employed to identify and replace erroneous vectors, including the replacement with displacement assessed from secondary peaks from the correlation map identified during the interrogation

**Table 1.** Roughness parameters of the biofilm-fouled plate and the smooth plate.

	$U_\tau$ (m s <sup>-1</sup> )	$\delta$ (mm)	$Re_\tau = \delta^+ = \delta U_\tau / \nu$	$U_\tau$ (m s <sup>-1</sup> )	$\Delta U^+$	$k_s^+$	$k_s$ (mm)	$C_f$
Smooth	1.2	33.5	$1.64 \times 10^3$	0.047	–	–	–	$2.9 \times 10^{-3}$
Biofilm	1.1	30.0	$2.5 \times 10^3$	0.076	12.8	736	8.8	$9.0 \times 10^{-3}$

$\delta^+$  is the friction Reynold number.

process. All instantaneous fields were then low-pass filtered with a narrow Gaussian filter to remove high-frequency noise. On average, between 1% and 2% of the velocity vectors were erroneous and therefore removed and interpolated across. A total of 4,000 statistically independent instantaneous velocity fields were acquired. The field-of-view (FOV) was  $2.4\delta \times 1.4\delta$  ( $\delta$  is the boundary layer thickness) and the final grid resolution was  $176 \mu\text{m}$ , allowing for 406 vertical velocity profiles in each frame, with between 262 and 264 velocity vectors per profile, depending on the height of the biofilm at that location. The boundary layer thickness,  $\delta$ , was measured from the lowest point of the biofilm in the PIV frame to the point with a mean velocity of 99% of the freestream value.

Additionally, smooth-wall boundary layer data over a non-fouled acrylic plate were taken in the same facility as the biofilm data and used for comparison in this study. Smooth wall measurements were taken slightly further from the trip than the biofilm measurements. Flow parameters for the smooth wall and slime-fouled wall are given in Table 1. Spatially explicit smooth-wall data are from PIV analysis as described above, with a  $2.3\delta \times 1.5\delta$  window. The spatial resolution of the smooth-wall PIV vector data was  $144 \mu\text{m}$ . For comparison, a smooth-wall mean velocity profile was taken using laser Doppler velocimetry (LDV) at the same location as PIV measurements. The LDV setup was similar to that described in Schultz and Flack (2007).

Two potential experimental problems should be addressed. First, the direction of flow during testing was perpendicular to the direction of flow during growth of the biofilms. Potentially, this results in streamers with a different morphology or mechanical properties than they would otherwise have. Under high speed unidirectional flow, biofilms form streamers described as dreadlock-type, with chains of diatoms tangling together to form the macroscopic streamers observed in biofilms grown under shear (Celler et al. 2014). Therefore, streamers formed under flow that is perpendicular to the test flow may not be as streamlined, thus increasing the drag more than streamers formed under the same flow regime as testing. However, the pliability of the streamers indicates that this effect is minimal. Additionally, this may not

be much divorced from real world scenarios of biofilm growth, which often occurs when a ship is in port, where water motion due to waves and currents also does not necessarily have the same direction as the ship's movement underway. For naval vessels especially, significant time is spent in port (Schultz 2004). A second potential concern is that testing was performed in freshwater, whereas biofilms were grown in brackish water (18 ppt). This may have resulted in some structural changes in the EPS, and death of the biofilm over the course of the experiment. However, one function of EPS is to protect cells from ionic and osmotic changes in their microhabitat (Decho 1990), potentially lessening the shock of the freshwater.

### Mean velocity profile analysis

The log-law equation for flow over a smooth wall,

$$U^+ = \frac{1}{\kappa} \ln(y^+) + C \quad (1)$$

describes the mean boundary layer velocity profile in the log region above the bed. Here, the + superscript indicates that the term is normalized by inner units ( $U_\tau$  or  $\frac{y}{U_\tau}$ ). Both  $C$  and  $\kappa$  are empirically derived universal constants.  $C$  is the log-law intercept for the smooth wall, here set to 5, and  $\kappa$  is the von Kármán constant, set to 0.41; this is the pair of values used by Volino et al. (2011). The structure of flow over a rough wall is altered, with the addition of a wall datum offset ( $\varepsilon$ ) and the roughness function ( $\Delta U^+$ ), so that the flow in the log-region of a rough wall boundary layer is described by

$$U^+ = \frac{1}{\kappa} \ln(y + \varepsilon)^+ + C - \Delta U^+ \quad (2)$$

where  $\Delta U^+$  represents the downward shift of the velocity profile in the log-law region (also called the roughness function), and  $\varepsilon$  is the vertical displacement of the virtual origin. The addition of these two variables complicates finding the friction velocity,  $U_\tau$ . Typically, an iterative procedure is used to adjust the values of  $U_\tau$  and  $\varepsilon$  until the slope matches that of the smooth wall (Perry & Li 1990). The boundary layer velocity profile in the outer region of the boundary layer can be described in the velocity defect form,

$$U_e^+ - U^+ = -\frac{1}{\kappa} \ln\left(\frac{y + \varepsilon}{\delta}\right) + \frac{2}{\kappa} \prod_k w(y/\delta) \quad (3)$$

where  $\frac{2}{\kappa} \prod_k w(y/\delta)$  is the Coles wake function (Coles 1956),  $\prod$  is the wake parameter, and  $w$  the wake function, which describes the departure of the mean velocity from the log-law in the outer layer. The wake function should be similar between the biofilm and the smooth wall, because the height of the biofilm is small compared to the thickness of the boundary layer (Jiménez 2004; Flack et al. 2007); in the present study  $k/\delta = 1/60$  (using the mean peak-to-trough distance of the biofilm for  $k$ ). Additionally, Walker et al. (2013b) found outer layer similarity over freshwater biofilm. Therefore, velocity defect similarity between the biofilm surface and a smooth wall was assumed in the present study (Flack et al. 2005, Castro 2007). A goodness-of-fit maximization scheme between the biofilm velocity defect profile and the smooth-wall velocity defect profile was used to calculate  $U_\tau$  and  $\varepsilon$  over the biofilm surface. To accomplish this, values of  $U_\tau$  and  $\varepsilon$  in Equation 3 were independently adjusted, and the combination resulting in the best fit between the biofilm and smooth wall profile was found. Finally,  $\Delta U^+$  was calculated by finding the value that resulted in the best match between the log and wake regions of the biofilm and smooth wall mean velocity profiles plotted in inner units. Because the biofilm is permeable, the initial origin was set at 0.5 mm below the bottom of the lowest trough of the biofilm in the PIV frame.

A modified Clauser chart method (as described in Schultz & Flack (2007)) was used to validate the velocity defect matching method (described above) for calculating the wall shear stress. The modified Clauser chart method uses an iterative procedure to calculate  $U_\tau$  by iteratively shifting  $\varepsilon$  and  $\Delta U^+$ , finding the best  $C_f$ , and repeating until optimized. The  $U_\tau$  values for the mean velocity profile calculated by the two methods were compared, as were the values of 4 local velocity profiles. The two methods yielded  $U_\tau$  values for the mean velocity profile that differed by 1.2%, and local  $U_\tau$  values that differed by an average of 3.2% and no more than 5.5%. In order to further validate the results, two additional fitting schemes were used with the mean velocity profile: One, an outer layer velocity defect matching scheme, was employed, where  $U_\tau$  is adjusted until the best fit between the smooth wall and biofilm velocity defect profile in the outer region ( $y > 0.19\delta$ ) is achieved; and two, a scheme that maximizes the fit of the smooth wall and biofilm profiles of both the velocity defect and the turbulence intensity ( $u'u'/U_\tau^2$ ) in the outer region, as

described in Monty et al. (2016). For both of these schemes, the  $\varepsilon$  was initially set at 0.5 mm to find the best fit, then  $\varepsilon$  and  $\Delta U^+$  were optimized to best fit the log-law region. The  $U_\tau$  values, as well as the  $\Delta U^+$  values, agreed with the results of our overlap region velocity defect matching within 3%.

The overlap region velocity defect matching method was employed to assess the friction velocities for the individual velocity profiles measured in this study because it could be more easily and reliably implemented in an optimization code than the modified Clauser chart method. The  $U_\tau$  value for the smooth wall was found using the modified Clauser method. The smooth wall LDV and PIV data gave slightly different  $U_\tau$  values ( $0.047 \text{ m s}^{-1}$  for the LDV data and  $0.049 \text{ m s}^{-1}$  for the PIV data).

## Results and discussion

### Mean velocity profile analysis

Figure 2 shows the mean velocity profile over the biofilm normalized using inner units (left panel) and outer units in velocity defect form (right panel), with the smooth-wall profile from both PIV and LDV for comparison. The turbulent boundary layer over the biofilm appears to exhibit a standard mean velocity profile, with a log-law region and the expected downward shift ( $\Delta U^+$ ) found in rough-wall flows (Figure 2A).

The downward shift in the log-law, also termed the roughness function, is  $\Delta U^+ = 12.8$ . This corresponds to a roughness Reynolds number of  $k_s^+ = 736$ , an order of magnitude higher than the threshold value of  $k_s^+ = 80$  given by Jimenez (2004) indicating that the flow is in the fully-rough regime (Table 1). This yields an equivalent sand-grain roughness height ( $k_s$ ) of 8.8 mm, meaning that the biofilm destroys the viscous sublayer, and the roughness effect on the mean flow is large. The  $k_s$  value was significantly larger than the

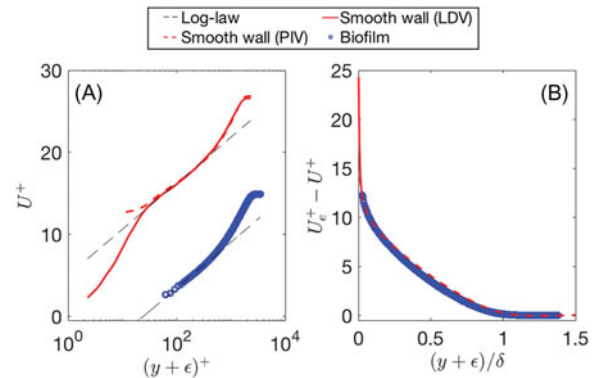
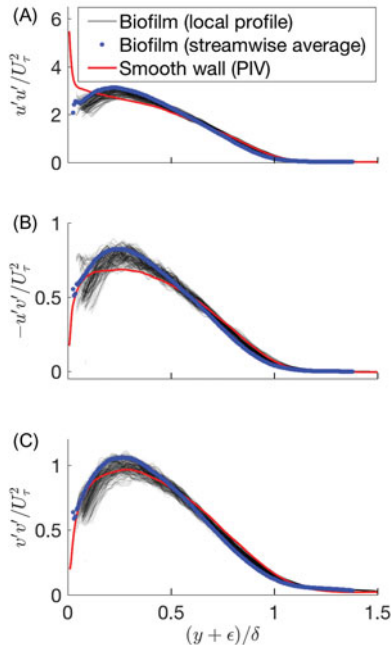


Figure 2. Average streamwise velocity profile over the biofilm and smooth wall in (A) inner units and (B) velocity defect form.

physical height of the biofilm (8.8 mm vs 1.7 mm), indicating that the flapping streamers and possibly the compliance of the biofilm layer may contribute to the large roughness effects of the biofilm. Additionally, the skin-friction coefficient ( $C_f = 2 \frac{U_\tau^2}{U_e^2}$ ) is significantly increased over the biofilm as compared to the smooth wall ( $9.0 \times 10^{-3}$  for the biofilm vs  $2.9 \times 10^{-3}$  for the smooth wall). However, when the biofilm mean velocity profile is presented in the defect form, a good collapse with the smooth-wall data is observed (Figure 2B). This outer layer similarity forms the basis of scaling techniques that aim to model the effects of surface roughness on vessel performance (Schultz 2007).

Figure 3 presents the streamwise averaged Reynolds stress profiles (blue circles), normalized in inner units, with smooth wall profiles (red line) for comparison. Additionally, the local profiles (normalized by the local  $U_\tau$  and  $\epsilon$  values) at each streamwise location in the PIV frame are shown (gray lines) to highlight the heterogeneities that the biofilm bed introduces in the roughness sublayer. The streamwise Reynolds stress (Figure 3A) over the biofilm shows significant changes compared with the smooth-wall condition in the roughness sub-layer region ( $y/\delta < 0.5$ ). The expected smooth-wall peak in  $\langle u'u' \rangle$  in the inner region is suppressed, possibly due to the high momentum deficit near the biofilm. Instead, a wider, weaker peak is seen at  $y/\delta \sim 0.3$ .



**Figure 3.** Average streamwise Reynolds stresses for the biofilm (blue circles) and smooth-wall (red lines) cases. The local values of the Reynolds stresses above the biofilm (gray lines) are also presented. (A)  $u'^2$ ; (B)  $-u'v'$ ; (C)  $v'^2$

The peak/plateau region in the Reynolds shear stress (RSS =  $-\langle u'v' \rangle$ ) over the biofilm is shifted away from the bed, has a sharper shape, and is elevated compared to the smooth wall (Figure 3B). The upward shift of the peak in both  $u'u'$  and  $u'v'$  is similarly seen over non-uniform biofilm fouling (Walker et al., 2013b), and is due to the relative increase in friction forces due to drag on the roughness elements and the resulting relative decrease in viscous forces. Finally, the streamwise averaged vertical Reynolds stress profile (Figure 3C; blue circles) has a slightly elevated peak compared with the smooth wall profile, however some individual profiles peak at lower values. It is worth pointing out that the streamwise averaged Reynolds stress profiles (blue circles) are located at the higher end of the range of the local profiles (gray lines) because they are normalized by the  $U_\tau$  calculated from the streamwise average velocity profile, which was slightly lower than most of the local  $U_\tau$  values, probably a result of error in  $U_\tau$  calculated from the local profiles. All the Reynolds stress profiles show good collapse in the outer layer.

### Spatially explicit mean flow analysis

Time-averaged streamwise ( $U$ ) and vertical ( $V$ ) velocity fields are presented in Figure 4, shown with smooth wall data for comparison and normalized using outer units ( $\delta$  and  $U_e$ ). The streamwise velocity over the biofilm exhibits a layer of low-momentum flow in the form of a momentum deficit that is evident just at the biofilm roughness layer when compared with the smooth-wall streamwise velocity field. Even though the variability of biofilm topography in the streamwise direction is considerable (masked white region below the contour values on Figure 4A), the mean streamwise velocity is quite homogeneous in the streamwise direction. In contrast, there is a striking increase in vertical velocity at the bed, as well as spatial heterogeneity in the vertical velocity over the biofilm.

Figure 5 shows the time-averaged RSS and turbulent kinetic energy ( $tke = \frac{1}{2}(u'^2 + v'^2)$ ), for both the biofouled and smooth wall, normalized by the free-stream velocity. The RSS fields (Figure 5 A, B & C) show an increase in shear stresses over the biofouled wall, as well as an upward shift in the location of the shear stress maximum. This is similar to what is seen in Figure 3B. There is also enhancement of the 2-D  $tke$  over the biofilm (Figure 5D, E & F). Like the RSS,  $tke$  also displays high streamwise spatial heterogeneity over the biofilm, and the core of  $tke$  ( $y/\delta > 0.1$  to  $y/$

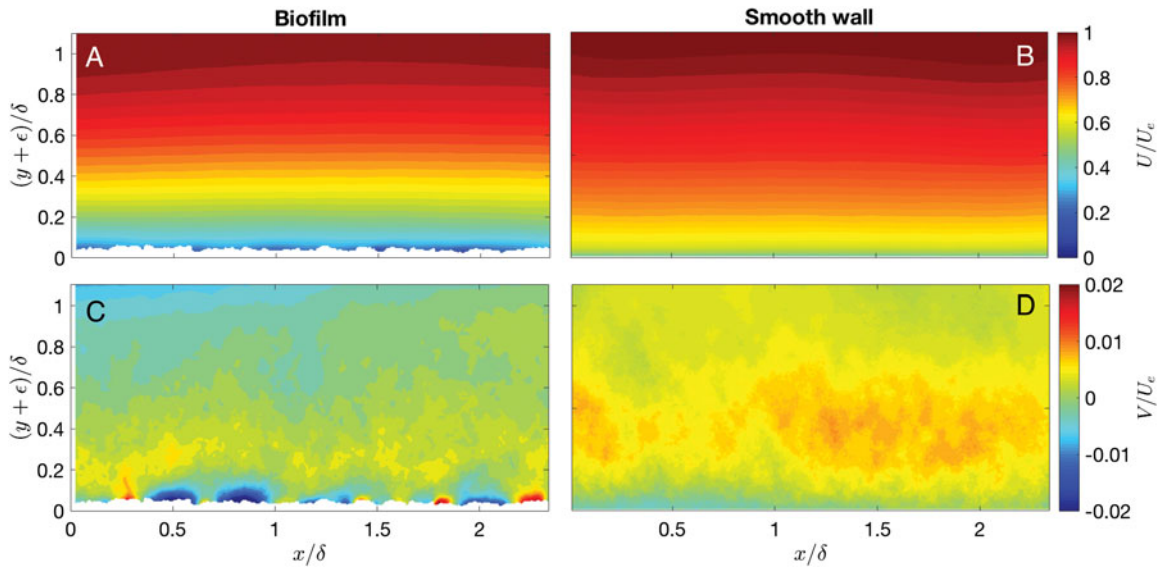


**Figure 4.** Time-averaged streamwise (A and B) and vertical (C and D) velocity over a biofilm (left panels) and smooth wall (right panels). Normalized with outer units: the freestream velocity,  $U_e$  and the boundary layer thickness,  $\delta$ .

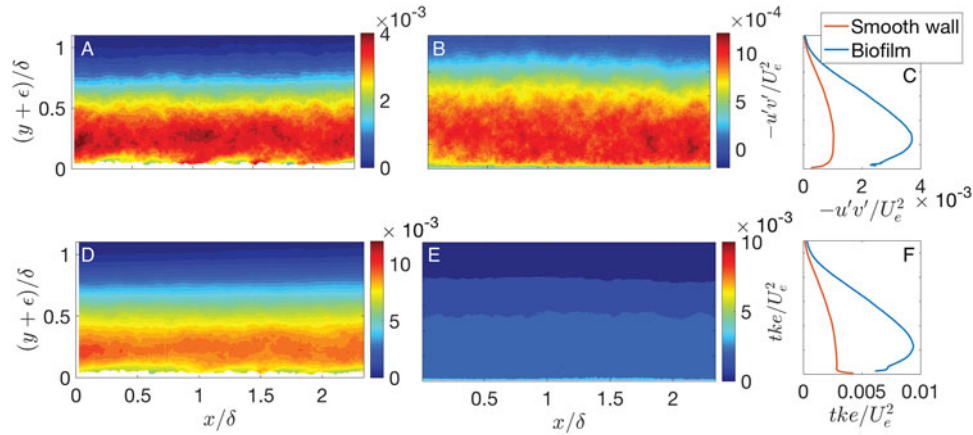


**Figure 5.** The 2D Reynolds shear stress (RSS) over the biofilm (A) and over the smooth wall (B) and the turbulent kinetic energy ( $tke$ ) over the biofilm (D) and the smooth wall (E), all normalized by the free stream velocity ( $U_e^2$ ). Note that the scale of the colorbars differ between the smooth wall and biofilm. To highlight the difference in magnitude of smooth wall and biofilm RSS and  $tke$  at different heights above the bed, streamwise averages of these values are also plotted (C & F). Note that here the y-axis is the  $\delta$  normalized height above the bed.

$\delta < 0.4$ ) is  $>3$  times greater than that of the smooth-wall case. The near bed hotspots of  $tke$  likely indicate increased turbulent transport and vertical mass and momentum transport (Reidenbach et al. 2010), which is important for transport of solutes to and from the bed. This suggests that even over a fairly uniform biofilm, enhancement of access to nutrients due to turbulence is locally variable.

Because of the spatial heterogeneity of the biofilm layer, it is also useful to perform a spatial decomposition of the velocity field

$$\tilde{u} = U - \langle U \rangle_\Lambda \quad (4)$$

where  $\langle U \rangle_\Lambda$  is the temporally and spatially (streamwise) averaged velocity field (Kevin et al. 2017). The

dispersive stresses are then  $\tilde{u}\tilde{v}$ . Dispersive stress fields illustrate where spatial variability in the flow, due to the surface topography, results in momentum transport (Coceal et al. 2006). Analysis of the dispersive stress is common in investigations of atmospheric flow over vegetation or urban surfaces, because the dispersive stress contributes to transport of scalar quantities, especially within sparse canopies (Poggi et al. 2004). Over the biofilm, hotspots of spatial variability in the flow are confined to the near-bed region (Figure 6A). These areas of elevated dispersive stresses seem to coincide with the downstream edges of the larger biofilm elements. The dispersive stresses are small compared to the RSS. In the near-bed region, the dispersive momentum flux,  $\tilde{u}\tilde{v}$ , reaches  $\sim 10\%$  of

the RSS. The production of *tke* ( $P = -u'v' \frac{\partial U}{\partial y}$ ) is also spatially heterogeneous (Figure 6B). There appears to be strong production of *tke* trailing behind many of the roughness elements of the biofilm. This is similarly seen in gravel beds, where enhanced *tke* production in the wake region behind protrusions results in strong turbulent interactions with the bed and increased vertical transport of mass and momentum (Mignot et al. 2009; Reidenbach et al. 2010).

### Spatial coherence analysis

Different types of roughness can have similar effects on the mean velocity profile (eg mesh and rods) (Krogstad & Antonia 1999), but different effects

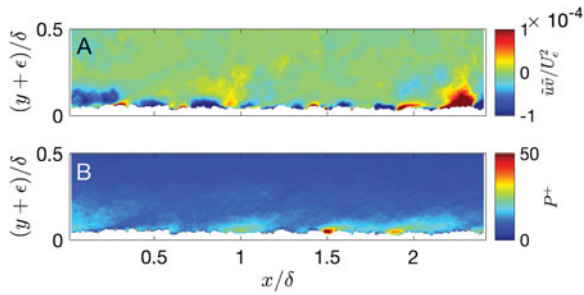


**Figure 6.** Dispersive stresses (A), normalized by  $U_e^2$  and (B) production of *tke* ( $P$ ), normalized by  $U_e^3/\delta$ . Each vertical profile of  $U$  was smoothed using a smoothing spline before finding  $\frac{\partial U}{\partial y}$  in  $P$ . Only the near-bed region is shown in order to highlight the spatial heterogeneity of the turbulence quantities.

on turbulence generation and turbulent stresses. For example, roughness alters the structure of the turbulence itself within the boundary layer, altering the size and coherence of vortices and the generation of turbulence at the wall (Volino et al. 2009; Wu & Christensen 2010; Mejia-Alvarez & Christensen 2010; Volino et al. 2011). However, little is known about how compliant roughness or flapping streamers alters this turbulence structure.

Coherent structures in the turbulent flow over the biofilm were assessed using three methods: two-point correlation, quadrant analysis, and the probability density function of the instantaneous RSS. The inhomogeneous two-point correlation in the streamwise-wall-normal plane is given as

$$\rho_{u_i u_j} = \frac{u_i(x_{ref}, y_{ref}) u_j(x_{ref} + \Delta x, y_{ref} + \Delta y)}{\sigma_{u_i}(x_{ref}, y_{ref}) \sigma_{u_j}(x_{ref} + \Delta x, y_{ref} + \Delta y)} \quad (5)$$

where  $\rho_{u_i u_j}$  is the two-point correlation normalized by the standard deviation of the local velocity and the reference velocity, and  $x_{ref}$  and  $y_{ref}$  denote the reference location. Here  $y_{ref} = 0.15\delta$  and  $x_{ref}$  was taken as the middle of the velocity field frame (Figure 7). For the streamwise correlation, the angle of inclination of  $\rho_{uu}$  (black line in Figures 7A & 7B) is an indication of the angle of the coherent structures that are shed from the wall (Christensen & Adrian 2001; Volino et al. 2007). The angle of inclination

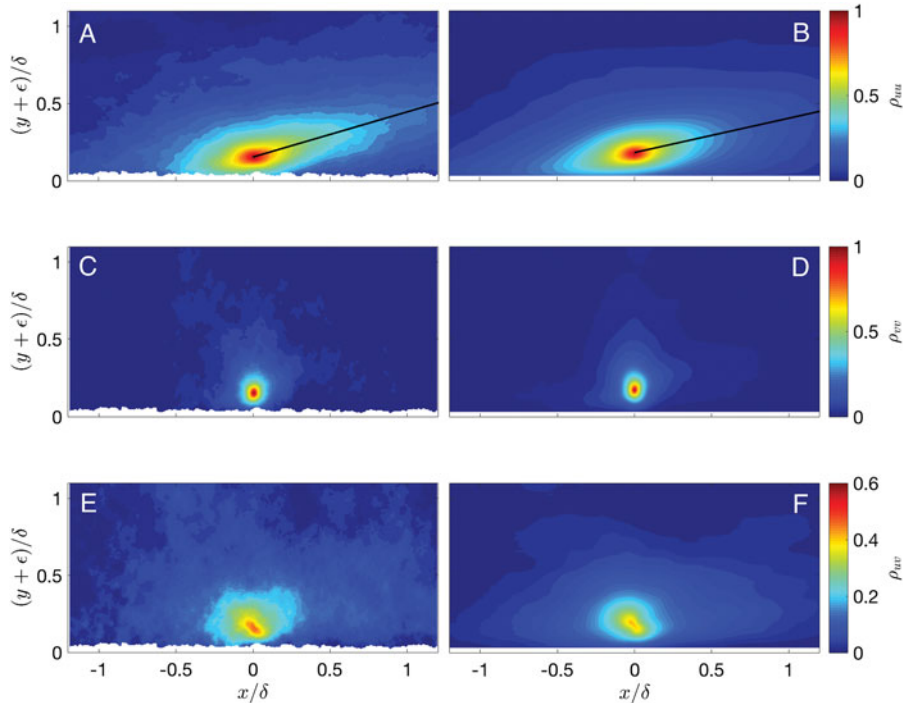


**Figure 7.** The two-point correlations,  $\rho_{uu}$  (A & B),  $\rho_{vv}$  (C & D) and  $\rho_{uv}$  (E & F), shown with data from a smooth wall for comparison. The black line in C and D marks the angle of inclination.

of  $\rho_{uu}$  is  $12.6^\circ$  for the smooth wall and  $16.5^\circ$  for the biofilm wall and was calculated by finding the point on each contour line that is furthest from the reference point and fitting a line through them. The slight increase in inclination angle over the biofilm may be due to increased vertical momentum transport over the biofilm bed. The streamwise- and wall-normal coherence of  $\rho_{uu}$  shows only a small qualitative difference between the smooth-wall and the biofilm flows. In both cases,  $\rho_{uu}$  is elongated in the streamwise direction. However, over the biofilm wall,  $\rho_{uu}$  appears to be slightly more elongated compared to the smooth wall, which is in contrast with several other rough-wall flows, where a reduction of the streamwise coherence of  $\rho_{uu}$  is seen (Volino et al. 2007; Wu & Christensen 2010). The shape of the wall-normal correlation,  $\rho_{vv}$ , is thought to be indicative of the size of the heads of hairpin packets (Wu & Christensen 2010). As has been shown in studies over other types of roughness, the shape of  $\rho_{vv}$  does not appear to be affected by the biofilm (Wu and Christensen 2010). The cross correlation  $\rho_{uv}$  also appears similar over the smooth wall and the biofilm.

Energy and momentum transport in turbulent wall bounded flow is hypothesized to be largely due to the presence of packets of hairpin vortices that entrain fluid and drive turbulent ejections and sweeps (Wu & Christensen 2010). The inclination angle of  $\rho_{uu}$  suggests that vortical structures in the flow move coherently away from the biofilm surface at a steeper angle than away from the smooth surface. However, qualitatively the two-point correlation maps look quite similar. Coherent vortical structures are important in the transport of turbulence in the boundary layer, especially the ejection of low-momentum fluid from near the bed into the outer layer (Moin & Kim 1985). Similarity in shape and angle of the streamwise correlation over the rough biofilm surface and the smooth wall has been seen over other types of 3-D roughness, both irregular (Wu & Christensen 2010) and regular (Volino et al. 2007), though these studies also find a small decrease in the streamwise length of the correlation ellipses. Similarity in the shape of  $\rho_{uv}$  over a rough and smooth surface was also observed in Volino et al. (2007). This and other studies, however, have shown a reduction in the streamwise length of contours of  $\rho_{vv}$  and  $\rho_{uv}$  with otherwise similar shapes (Wu & Christensen 2010), which is thought to be due to a decrease in the length scales of large-scale groupings of vortices over rough surfaces. The present results suggest that the biofilm surface increases the coherence of the turbulence slightly,

whereas rigid roughness tends to decrease it. The potentially altered energy and momentum transport in the biofilm flow compared to rigid roughness may have to do with the way eddies are shed off of the cell clusters, causing three-dimensional flapping of the streamers (Stoodley et al. 1998). The 2-D PIV used here is likely to oversimplify the three dimensional nature of the flow structure and coherence, especially given the flapping streamers. In the future, 3-D PIV or PTV (Particle Tracking Velocimetry) could be used to better resolve the dynamics of vortex shedding.

### Quadrant analysis

Quadrant analysis is used to measure the relative contribution of instantaneous turbulent sweeps ( $Q_4$ ; where  $u' > 0, v' < 0$ ) and ejections ( $Q_2$ ; where  $u' < 0, v' > 0$ ) to the overall RSS field. The Quadrant-Hole technique was used to identify only the contribution of high-magnitude instantaneous events (Lu & Willmarth, 1973). The time-averaged  $Q_2$  and  $Q_4$  fields are presented in Figure 8 and were calculated by taking the conditional average of local instantaneous events where

$$|u'v'| > H\sigma_u\sigma_v \quad (6)$$

with, here,  $\sigma_{u_i} = \sqrt{\langle u_i'^2 \rangle}$  and a hyperbolic hole of size  $H=4$ . Only the results for  $Q_2$  and  $Q_4$  are given, as the contributions of  $Q_1$  and  $Q_3$  events (where  $u'v' > 0$ ) are negligible. The Quadrant-Hole results indicate that strong turbulent sweeps are the primary contributors to the RSS near the biofilm surface (Figure 8B), while turbulent ejections become more dominant further from the bed (Figure 8A). This means that there is significant downrushing of high momentum fluid from further up in the boundary layer toward the bed. This  $Q_4$  dominance at the bed may in large part be due to prograde vortices (i.e. vortices rotating with the mean shear) being shed off of the biofilm clusters and streamers. This is

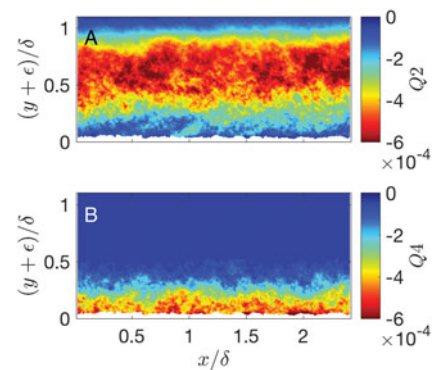
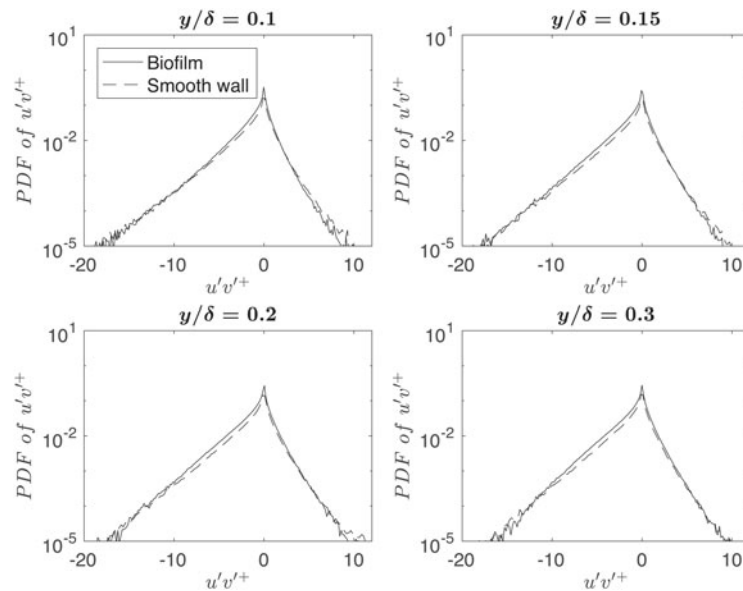


Figure 8. The time-averaged contributions of turbulent ejections ( $Q_2$ ; A) and sweeps ( $Q_4$ ; B) with  $H=4$ .



**Figure 9.** The probability density function of the instantaneous RSS over the biofilm (solid line) and smooth wall (dashed line; from PIV data) at four different heights above the bed.

observed above canopy flows, where prograde vortices shed off of flexible seagrass analogs have strong downward momentum and weaker upward momentum at the top of the canopy (Raupach et al. 1991; Ghisalberti & Nepf 2006; Hansen & Reidenbach 2017). There is also significant streamwise spatial heterogeneity in the strength of sweeps and ejections, because these turbulent events are a result of the bed topography.

The probability density function (PDF) of instantaneous RSS is another useful way to quantify the dominant structures of turbulent flow over the biofilm (Figure 9), here presented at four different  $y/\delta$  positions above the biofilm, along with the RSS PDFs over the smooth wall. It appears that the RSS contributions are similar between the smooth wall and biofilm, and are similar at the different heights over the wall. Over rigid roughness, large 2-D roughness elements tend to have the most divergence in the RSS PDF from the smooth wall, while large and small 3-D roughness elements are far more similar (Volino et al. 2011). Because the biofilm is highly three dimensional, the results shown in Figure 9 fit with previously observed behavior.

## Conclusions

The aim of this study was to address the mechanisms resulting in high drag due to low form, compliant biofilms. To accomplish this, the study addressed the spatially resolved turbulence structure over a biofilm at low Reynolds number. The results show that biofilms extract energy from the flow through the

roughness of the biofilm surface as well as the flapping streamers, resulting in a larger effective roughness height than the physical roughness. Additionally, there is large spatial heterogeneity in the turbulence and momentum transport over the bed even though the biofilm was relatively uniform in coverage.

Generally, the mean statistics of the biofilm-fouled surface behaved similarly to a rigid rough wall. Turbulent kinetic energy production appeared dominant at discrete locations along the bed (Figure 5D). Near bed local variability in turbulence production (Figure 6B) and momentum fluxes (Figure 8) indicate that while outer layer similarity was maintained over a biofilm, small scale turbulence structures near the bed, which are important for transport of nutrients to sessile biofilms as well as the hydrodynamic forces that slough biofilm off the surface, were altered by local bed topography created by the biofilm. This dynamic is also observed over coral reefs, where the roughness effects of the reef as a whole determine integrated flow characteristics such as drag coefficient and shear, but at the organismal scale local topography impacts biologically relevant hydrodynamics (Reidenbach et al. 2006). Biofilm growth is highly dependent on fluid motion, even more so than light environment or nutrient concentration (Hondzo & Wang 2002), and it may be that biofilms favor a highly turbulent near-bed hydrodynamic regime, leading to increased vertical transport of nutrients to the biofilm, and transport of metabolic byproducts from the biofilm. Although this increase in vertical transport is likely beneficial to the biofilm community the

increase in shear stresses may also lead to sloughing of the biofilm. Ships' hulls can exhibit sparse or patchy slime fouling. This variability in the physical structure of the biofilm was not addressed in the present work, in order to gain a baseline understanding of flow over a biofilm, but future studies should address the hydrodynamic impacts of patchy biofilms. The added surface roughness due to the biofilm, despite the low vertical relief, results in increased drag due to high levels of momentum transport likely due to flapping streamers and surface compliance. Integrated over a large surface such as a ship hull, this can result in significant drag penalties.

## Acknowledgements

The authors thank three anonymous reviewers for insightful comments and criticism which improved this manuscript. The authors are also grateful to the staff of the USNA Hydromechanics Lab, especially Mark Pavkov, Dan Rhodes and Michael Stanbro, for technical support and care and maintenance of the dynamic slime facility.

## Disclosure statement

No potential conflict of interest was reported by the authors.

## Data availability statement

The data from this study are openly available in the data repository Zenodo at <https://doi.org/10.5281/zenodo.1175014>

## Funding

This work was supported by the US Office of Naval Research Grant #N0001417-WX-00846; the US Office of Naval Research Grant #N00014-15-1-2560; the US National Science Foundation Graduate Research Internship Program Fellowship #2014162109; and the US National Science Foundation Graduate Research Fellowship Program #DDGE-1315231.

## ORCID

Elizabeth A. K. Murphy  <http://orcid.org/0000-0003-3316-7328>

Julio M. Barros  <https://orcid.org/0000-0003-4283-2262>

Matthew A. Reidenbach  <https://orcid.org/0000-0002-5592-920X>

## References

Castro IP. 2007. Rough-wall boundary layers: mean flow universality. *J Fluid Mech.* 585:469–485. doi:10.1017/S0022112007006921

- Celler K, Hödl I, Simone A, Battin TJ, Picioreanu C. 2014. A mass-spring model unveils the morphogenesis of phototrophic *Diatoma* biofilms. *Sci Rep.* 4:3649. doi:10.1038/srep03649
- Christensen KT, Adrian RJ. 2001. Statistical evidence of hairpin packets in wall turbulence. *J Fluid Mech.* 431:433–443. doi:10.1017/S0022112001003512
- Coccali O, Thomas TG, Castro IP, Belcher SE. 2006. Mean flow and turbulence statistics over groups of urban-like cubical obstacles. *Bound-Layer Meteorol.* 121:491–519. doi:10.1007/s10546-006-9076-2
- Coles D. 1956. The law of the wake in the turbulent boundary layer. *J Fluid Mech.* 1:191–226. doi:10.1017/S0022112056000135
- de Beer D, Kühl M. 2001. Interfacial microbial mats and biofilms. In: Boudreau BP, Jørgensen BB, editors. *The benthic boundary layer.* Oxford University Press, Inc. Oxford, UK.
- de Beer D, Stoodley P, Lewandowski Z. 1996. Liquid flow and mass transport in heterogeneous biofilms. *Water Res.* 30:2761–2765. doi:10.1016/S0043-1354(96)00141-8
- Decho AW. 1990. Microbial exopolymer secretions in ocean environments: their role(s) in food webs and marine processes. *Oceanogr Mar Biol Annu Rev.* 28:73–153.
- Flack KA, Schultz MP. 2010. Review of hydraulic roughness scales in the fully rough regime. *J Fluids Eng.* 132:041203. doi:10.1115/1.4001492
- Flack KA, Schultz MP, Shapiro TA. 2005. Experimental support for Townsend's Reynolds number similarity hypothesis on rough walls. *Phys Fluids.* 17:035102. doi:10.1063/1.1843135
- Flack KA, Schultz MP, Connelly JS. 2007. Examination of a critical roughness height for outer layer similarity. *Phys Fluids.* 19:095104. doi:10.1063/1.2757708
- Ghisalberti M, Nepf H. 2006. The structure of the shear layer in flows over rigid and flexible canopies. *Envl Mech.* 6:277–301. doi:10.1007/s10652-006-0002-4
- Graba M, Moulin FY, Boulétreau S, Garabétian F, Kettab A, Eiff O, Sánchez-Pérez JM, Sauvage S. 2010. Effect of near-bed turbulence on chronic detachment of epilithic biofilm: experimental and modeling approaches. *Water Resour Res.* 46:W11531. doi:10.1029/2009WR008679
- Hansen JCR, Reidenbach MA. 2017. Turbulent mixing and fluid transport within Florida Bay seagrass meadows. *Adv Water Resour.* 108:205–215. doi:10.1016/j.advwatres.2017.08.001
- Haslbeck EG, Bohlander G. 1992. Microbial biofilm effects on drag- lab and field. In: *Proceedings of the SNAME Ship Production Symposium.* Paper No. 3A-1. Jersey City, NJ: SNAME; 7p.
- Hondzo M, Wang H. 2002. Effects of turbulence on growth and metabolism of periphyton in a laboratory flume. *Water Resour Res.* 38:1277. doi:10.1029/2002WR001409
- Hunsucker KZ, Koka A, Lund G, Swain GW. 2014. Diatom community structure on in-service cruise ship hulls. *Biofouling.* 30:1133–1140. doi:10.1080/08927014.2014.974576
- Hunsucker KZ, Vora GJ, Hunsucker JT, Gardner H, Leary DH, Kim S, Lin B, Swain GW. 2018. Biofilm community structure and the associated drag penalties of a groomed fouling release ship hull coating. *Biofouling.* 34:162–72. doi:10.1080/08927014.2017.1417395

- Jiménez J. 2004. Turbulent flows over rough walls. *Annu Rev Fluid Mech.* 36:173–196. doi:10.1146/annurev.fluid.36.050802.122103
- Kevin K, Monty JP, Bai HL, Pathikonda G, Nugroho B, Barros JM, Christensen KT, Hutchins N. 2017. Cross-stream stereoscopic particle image velocimetry of a modified turbulent boundary layer over directional surface pattern. *J Fluid Mech.* 813:412–435. doi:10.1017/jfm.2016.879
- Krogstad PÅ, Antonia RA. 1999. Surface roughness effects in turbulent boundary layers. *Exp Fluids.* 27:450–460. doi:10.1007/s003480050370
- Lewthwaite JC, Molland AF, Thomas KW. 1985. An investigation into the variation of ship skin frictional resistance with fouling. *Trans R Inst Naval Architects.* 127:269–284.
- Lu SS, Willmarth WW. 1973. Measurements of the structure of the Reynolds stress in a turbulent boundary layer. *J Fluid Mech.* 60:481–511. doi:10.1017/S0022112073000315
- Mejia-Alvarez R, Christensen KT. 2010. Low-order representations of irregular surface roughness and their impact on a turbulent boundary layer. *Phys Fluids.* 22:015106. doi:10.1063/1.3291076
- Mignot E, Hurther D, Barthelemy E. 2009. On the structure of shear stress and turbulent kinetic energy flux across the roughness layer of a gravel-bed channel flow. *J Fluid Mech.* 638:423–452. doi:10.1017/S0022112009990772
- Moin P, Kim J. 1985. The structure of the vorticity field in turbulent channel flow. Part 1: Analysis of instantaneous fields and statistical correlations. *J Fluid Mech.* 155:441–464. doi:10.1017/S0022112085001896
- Molino PJ, Wetherbee R. 2008. The biology of biofouling diatoms and their role in the development of microbial slimes. *Biofouling.* 24:365–379. doi:10.1080/08927010802254583
- Monty JP, Dogan E, Hanson R, Scardino AJ, Ganapathisubramani B, Hutchins N. 2016. An assessment of the ship drag penalty arising from light calcareous tubeworm fouling. *Biofouling.* 32:451–464. doi:10.1080/08927014.2016.1148140
- Munk T, Kane D, Yebra DM. 2009. The effects of corrosion and fouling on the performance of ocean-going vessels: a naval architectural perspective. In: Hellio C, Yebra PM, editors. *Advances in marine antifouling coatings and technologies.* CRC Press. Cambridge, UK. 209–235.
- Murphy EAK, Barros JM, Schultz MP, Flack KA, Steppe CN, Reidenbach MA. 2017. The turbulent boundary layer structure over diatomaceous slime fouling. In: *Proceedings of the 10th International Symposium on Turbulence and Shear Flow Phenomena*, vol. 1, 3D-4. Chicago, USA.
- Nikora VI, Goring DG, Biggs BJ. 2002. Some observations of the effects of micro-organisms growing on the bed of an open channel on the turbulence properties. *J Fluid Mech.* 450:317–341. doi:10.1017/S0022112001006486
- Nikuradse J. 1933. Laws of flow in rough pipes. NACA Technical Memorandum 1292.
- Perry AE, Li JD. 1990. Experimental support for the attached-eddy hypothesis in zero-pressure-gradient turbulent boundary layers. *J Fluid Mech.* 218:405–438. doi:10.1017/S0022112090001057
- Picologlou BF, Zelter N, Characklis WG. 1980. Biofilm growth and hydraulic performance. *ASCE J Hydraulics Div.* 106:733–746.
- Poggi D, Katul GG, Albertson JD. 2004. A note on the contribution of dispersive fluxes to momentum transfer within canopies. *Bound-Layer Meteor.* 111:615–621. doi:10.1023/B:BOUN.0000016563.76874.47
- Raupach MR, Antonia RA, Rajagopalan S. 1991. Rough-wall turbulent boundary layers. *Appl Mech Rev.* 44:1–25. doi:10.1115/1.3119492
- Reidenbach MA, Limm M, Hondzo M, Stacey MT. 2010. Effects of bed roughness on boundary layer mixing and mass flux across the sediment-water interface. *Water Resour Res.* 46:W07530. doi:10.1029/2009WR008248
- Reidenbach MA, Monismith SG, Koseff JR, Yahel G, Genin A. 2006. Boundary layer turbulence and flow structure over a fringing coral reef. *Limnol Oceanogr.* 51:1956–1968. doi:10.4319/lo.2006.51.5.1956
- Schultz MP. 2004. Frictional resistance of antifouling coating systems. *J Fluids Engin.* 126:1039–1047. doi:10.1115/1.1845552
- Schultz MP. 2007. Effects of coating roughness and biofouling on ship resistance and powering. *Biofouling.* 23:331–341. doi:10.1080/08927010701461974
- Schultz MP, Flack KA. 2007. The rough-wall turbulent boundary layer from the hydraulically smooth to the fully rough regime. *J Fluid Mech.* 580:381–405. doi:10.1017/S0022112007005502
- Schultz MP, Bendick JA, Holm ER, Hertel WM. 2011. Economic impact of biofouling on a Naval surface ship. *Biofouling.* 27:87–98. doi:10.1080/08927014.2010.542809
- Schultz MP, Walker JM, Steppe CN, Flack KA. 2015. Impact of diatomaceous biofilms on the frictional drag of fouling-release coatings. *Biofouling.* 31:759–773. doi:10.1080/08927014.2015.1108407
- Stocking JB, Rippe JP, Reidenbach MA. 2016. Structure and dynamics of turbulent boundary layer flow over healthy and algae-covered corals. *Coral Reefs.* 35:1047–1059. doi:10.1007/s00338-016-1446-8
- Stoodley P, Lewandowski Z, Boyle JD, Lappin-Scott HM. 1998. Oscillation characteristics of biofilm streamers in turbulent flowing water as related to drag and pressure drop. *Biotechnol Bioeng.* 57:536–544.
- Stoodley P, Lewandowski Z, Boyle JD, Lappin-Scott HM. 1999. Structural deformation of bacterial biofilms caused by short-term fluctuations in fluid shear: An *in situ* investigation of biofilm rheology. *Biotechnol Bioeng.* 65:83–92. doi:10.1002/(SICI)1097-0290(19991005)65:1<83::AID-BIT10>3.0.CO;2-B
- Swain GW, Kovach B, Touzot A, Casse F, Kavanagh CJ. 2007. Measuring the performance of today's antifouling coatings. *J Ship Prod.* 23:164–170.
- Taherzadeh D, Picioreanu C, Küttler U, Simone A, Wall WA, Horn H. 2009. Computational study of the drag and oscillatory movement of biofilm streamers in fast flows. *Biotechnol Bioeng.* 105:600–610. doi:10.1002/bit.22551
- Townsin RL. 2003. The ship hull fouling penalty. *Biofouling.* 19:9–15. doi:10.1080/0892701031000088535
- U.S. Navy. 2006. *Naval Ships' Technical Manual*, Chapter 081. Waterborne underwater hull cleaning of navy ships. Oct 1, Revision 5. Direction of Commander, Naval Sea Systems Command. S9086-CQ-STM-010.
- Volino RJ, Schultz MP, Flack KA. 2007. Turbulence structure in rough- and smooth-wall boundary layers. *J Fluid Mech.* 592:263–293. doi:10.1017/S0022112007008518
- Volino RJ, Schultz MP, Flack KA. 2009. Turbulence structure in a boundary layer with two-dimensional

- roughness. *J Fluid Mech.* 635:75–101. doi:[10.1017/S0022112009007617](https://doi.org/10.1017/S0022112009007617)
- Volino RJ, Schultz MP, Flack KA. 2011. Turbulence structure in boundary layers over periodic two- and three-dimensional roughness. *J Fluid Mech.* 676:172–190. doi:[10.1017/S0022112011000383](https://doi.org/10.1017/S0022112011000383)
- Walker JM, Flack KA, Lust EE, Schultz MP, Luznik L. 2013a. Experimental and numerical studies of blade roughness and fouling on marine current turbine performance. *Renew Energ.* 66:257–267. doi:[10.1016/j.renene.2013.12.012](https://doi.org/10.1016/j.renene.2013.12.012)
- Walker JM, Sargison JE, Henderson AD. 2013b. Turbulent boundary-layer structure of flows over freshwater biofilms. *Exp Fluids.* 54:1628. doi:[10.1007/s00348-013-1628-x](https://doi.org/10.1007/s00348-013-1628-x)
- Wu Y, Christensen KT. 2010. Spatial structure of a turbulent boundary layer with irregular surface roughness. *J Fluid Mech.* 655:380–418. doi:[10.1017/S0022112010000960](https://doi.org/10.1017/S0022112010000960)
- Xu S, Rempfer D, Lumley J. 2003. Turbulence over a compliant surface: numerical simulation and analysis. *J Fluid Mech.* 478:11–34. doi:[10.1017/S0022112002003324](https://doi.org/10.1017/S0022112002003324)
- Zargiel KA, Coogan JS, Swain GW. 2011. Diatom community structure on commercially available ship hull coatings. *Biofouling.* 27:955–965. doi:[10.1080/08927014.2011.618268](https://doi.org/10.1080/08927014.2011.618268)
- Zargiel KA, Swain GW. 2014. Static versus dynamic settlement and adhesion of diatoms to ship hull coatings. *Biofouling* 30:115–129. doi:[10.1080/08927014.2013.847927](https://doi.org/10.1080/08927014.2013.847927)